

Lattice thermal conductivity of Bi, Sb, and Bi-Sb alloy from first principles

Sangyeop Lee,¹ Keivan Esfarjani,^{2,3} Jonathan Mendoza,¹ Mildred S. Dresselhaus,^{4,5} and Gang Chen¹

¹*Department of Mechanical Engineering, Massachusetts Institute of Technology, Cambridge, MA 02139, USA*

²*Department of Mechanical and Aerospace Engineering, Rutgers University, New Brunswick, NJ 08901, USA*

³*Institute for Advanced Materials and Devices for Nanotechnology (IAMDN), Rutgers University, Piscataway, NJ 08854, USA*

⁴*Department of Electrical Engineering and Computer Science, Massachusetts Institute of Technology, Cambridge, MA 02139, USA*

⁵*Department of Physics, Massachusetts Institute of Technology, Cambridge, MA 02139, USA*

(Received 20 December 2013; revised manuscript received 12 February 2014; published 25 February 2014)

Using first principles, we calculate the lattice thermal conductivity of Bi, Sb, and Bi-Sb alloys, which are of great importance for thermoelectric and thermomagnetic cooling applications. Our calculation reveals that the ninth-neighbor harmonic and anharmonic force constants are significant; accordingly, they largely affect the lattice thermal conductivity. Several features of the thermal transport in these materials are studied: (1) the relative contributions from phonons and electrons to the total thermal conductivity as a function of temperature are estimated by comparing the calculated lattice thermal conductivity to the measured total thermal conductivity, (2) the anisotropy of the lattice thermal conductivity is calculated and compared to that of the electronic contribution in Bi, and (3) the phonon mean free path distributions, which are useful for developing nanostructures to reduce the lattice thermal conductivity, are calculated. The phonon mean free paths are found to range from 10 to 100 nm for Bi at 100 K.

DOI: [10.1103/PhysRevB.89.085206](https://doi.org/10.1103/PhysRevB.89.085206)

PACS number(s): 63.20.kg, 66.70.-f

I. INTRODUCTION

Bi and Bi-Sb alloys have long been studied for their promising low-temperature thermoelectric applications. Bi and Sb have a rhombohedral crystal structure, which is a Peierl distortion of the simple cubic crystal. The small structural distortion results in Brillouin zone folding and a small overlap between conduction and valence bands, thereby causing semimetallic behavior and conduction by both electrons and holes. Since the semimetallic behavior causes cancellation of the hole and electron contributions to the power factor, bulk Bi is not a good thermoelectric material. However, Bi has a large thermomagnetic effect and a large thermomagnetic figure of merit (ZT) [1]. The thermomagnetic effect is particularly pronounced below 10 K due to the extremely long mean free path of the electrons in Bi [2]. In addition, Bi nanowires become semiconducting as their diameters approach several nanometers, thereby exhibiting a large thermoelectric power factor [3,4]. As a conventional bulk thermoelectric material, $\text{Bi}_{1-x}\text{Sb}_x$ has drawn more attention than Bi, since alloying with a small amount of Sb causes $\text{Bi}_{1-x}\text{Sb}_x$ to become a narrow gap semiconductor, which is advantageous for high thermoelectric efficiency. Currently, $\text{Bi}_{1-x}\text{Sb}_x$ ($x \approx 0.12$) is the best n -type thermoelectric material below 200 K [5].

Before discussing the lattice thermal transport, we emphasize that electrons, in addition to phonons, carry a considerable amount of heat in Bi, Sb, and Bi-Sb alloys. Therefore, both phonons and electrons contribute to the total thermal conductivity, which can be expressed as

$$\kappa_{\text{tot}} = \kappa_{\text{ph}} + \kappa_{\text{e}} \quad (1)$$

where κ_{tot} and κ_{ph} are the total thermal conductivity and the lattice thermal conductivity, respectively. The term κ_{e} includes the thermal conductivity of electrons and holes, as well as the bipolar contribution. The κ_{e} of Bi, Sb, and Bi-Sb alloys is expected to contribute substantially to κ_{tot} , since these

materials are either semimetals or semiconductors with a very narrow band gap.

Accurate methods to obtain separate κ_{ph} and κ_{e} are crucial to developing better thermoelectric materials, but separating κ_{ph} and κ_{e} is experimentally nontrivial. κ_{ph} can be directly measured under a high magnetic field, because such fields largely suppress electron transport. Previous measurements [6,7] in practical temperature ranges (100–300 K) utilized this method, but the prior measurements are mainly limited to transport along the binary crystallographic direction. We could not find any reports on κ_{ph} along the trigonal direction, which is expected to have a greater ZT than for the binary direction and thus is of more interest. Another way to separate κ_{ph} and κ_{e} is to estimate κ_{e} using either the Wiedemann-Franz law or other electron transport properties, such as the electrical conductivity and Seebeck coefficient [8]. Such an approach provides a reasonable qualitative analysis, but validity of the Wiedemann-Franz law and the simple electron transport models used in the estimation of κ_{e} is sometimes questionable for quantitative purposes [9].

In this paper, we study the lattice dynamics and quantify κ_{ph} for Bi, Sb, and Bi-Sb alloys from first principles and the Boltzmann transport equation. As shown in recent papers [10–16], this approach provides excellent agreement with experimental data for many pair-bonded materials, such as Si, GaAs, and Si-Ge alloys. We follow the same approach but pay special attention to the range of interatomic interactions. This is because Bi, unlike pair-bonded materials, has significant interaction strength out to large number neighbors, such as the ninth-nearest neighbor [17,18].

II. SECOND- AND THIRD-ORDER FORCE CONSTANTS

In this paper, we calculated the second- and third-order force constants using density functional theory. The calculation of the second-order force constants of Bi and Sb is based on the real space approach [19]. We calculated the force exerted

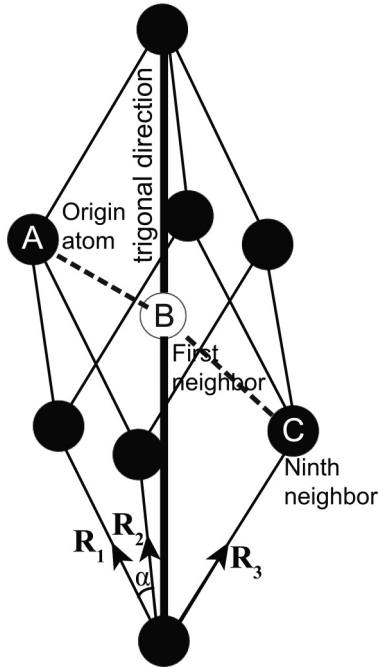


FIG. 1. Crystal structure of Bi and Sb. The void and filled atoms represent two basis atoms. R_1 , R_2 , and R_3 are primitive lattice vectors, and α is a rhombohedral angle. The values of α are $57^\circ 30'$ for Bi and $57^\circ 84'$ for Sb, which are close to 60° for the simple cubic structure.

on each atom when we displace one or multiple atoms in a $4 \times 4 \times 4$ supercell (128 atoms). For the supercell calculation, we used 30 Ry for the cutoff energy of the plane wave basis and a $4 \times 4 \times 4$ k -point mesh for Brillouin zone sampling, both of which were carefully checked for convergence. The calculation was performed with the ABINIT package [20] and Hartwigsen-Goedecker-Hutter pseudopotentials [21]. The valence electrons in the pseudopotential are $6s^2 6p^3$ and $5s^2 5p^3$ for Bi and Sb, respectively. The spin-orbit interaction is included in all calculations because of the strong spin-orbit interaction in Bi and Sb [22]. The second-order force constants are then fitted to the calculated displacement-force data set while enforcing translational and rotational invariance. In the fitting process, we considered up to the 14th neighbors to include the previously reported long-ranged interaction occurring at the ninth neighbor [17,18]. The ninth neighbors are shown by the atom labeled C in Fig. 1, where the origin atom is described by atom A. Bi and Sb both have a slightly distorted simple cubic crystal structure. Due to this small crystallographic distortion, the six first neighbors in the cubic structure become three first neighbors and three second neighbors. In Fig. 1, atom B is the first neighbor to atom A and the second neighbor to atom C. The almost collinear chain consisting of AB and BC forms the ninth-neighbor relation, and atom C is the ninth neighbor to atom A. In the following discussions, the fourth and ninth neighbors are frequently mentioned to discuss the range of the force constants. The fourth and ninth neighbors in the rhombohedral crystal structure of Bi correspond to the second neighbor (separated by $\sqrt{2}a$) and the fourth neighbor (separated by $2a$), respectively, in the undistorted cubic structure, where a is the lattice constant of the simple cubic structure.

The third-order force constants were calculated by taking finite differences of the second-order force constants [23]. We built a $3 \times 3 \times 3$ supercell consisting of 54 atoms, and we displaced one of the two basis atoms along the $+R_1$ direction in Fig. 1 by 0.04 \AA . The displacement value of 0.04 \AA was chosen after carefully checking the convergence of third-order force constants with respect to the displacement values. The size of the supercell was large enough to include the significant ninth-neighbor interaction. In addition, the large size of the supercell minimizes the effect from the periodic images of the displaced atom due to periodic boundary conditions. For the calculation, a cutoff energy of 30 Ry and a $3 \times 3 \times 3$ k -point mesh are used. We then calculate the second-order force constants using density functional perturbation theory [24,25]. All of the procedures are repeated for another supercell with the displacement along the $-R_1$ direction. By taking the finite differences of the second-order force constants of the two different supercells, the third-order force constants with respect to the R_1 direction are calculated. Rotational invariance with respect to the trigonal direction is then applied to calculate the third-order force constants with respect to the R_2 and R_3 directions. Translational invariance is applied to the third-order force constants by modifying the self-interaction terms.

We calculated phonon dispersions and mode Grüneisen parameters to validate the calculated second- and third-order force constants. In Fig. 2(a), we plot the trace of the

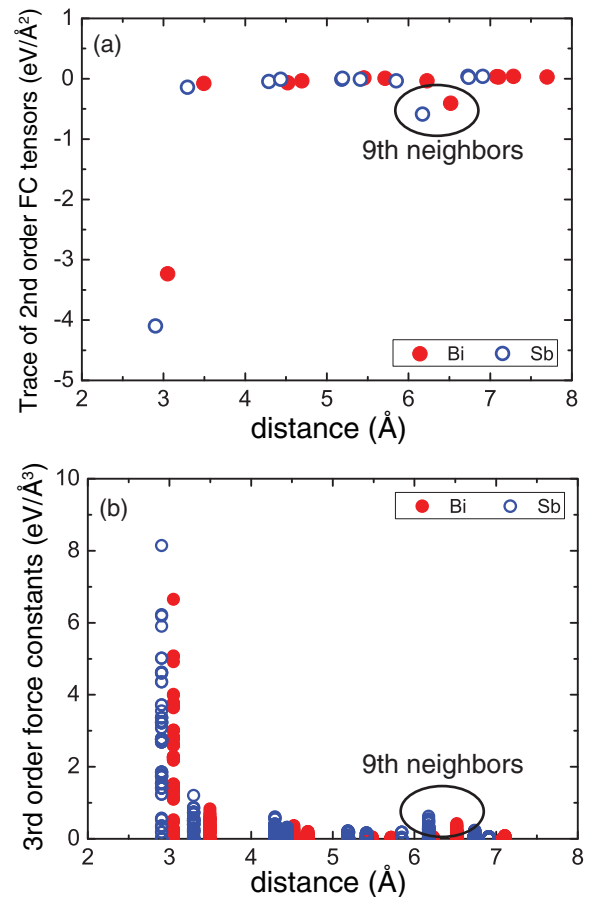


FIG. 2. (Color online) Force constants (FCs) of Bi and Sb versus interatomic distance: (a) Trace values of second-order FC tensors and (b) two-body third-order FCs.

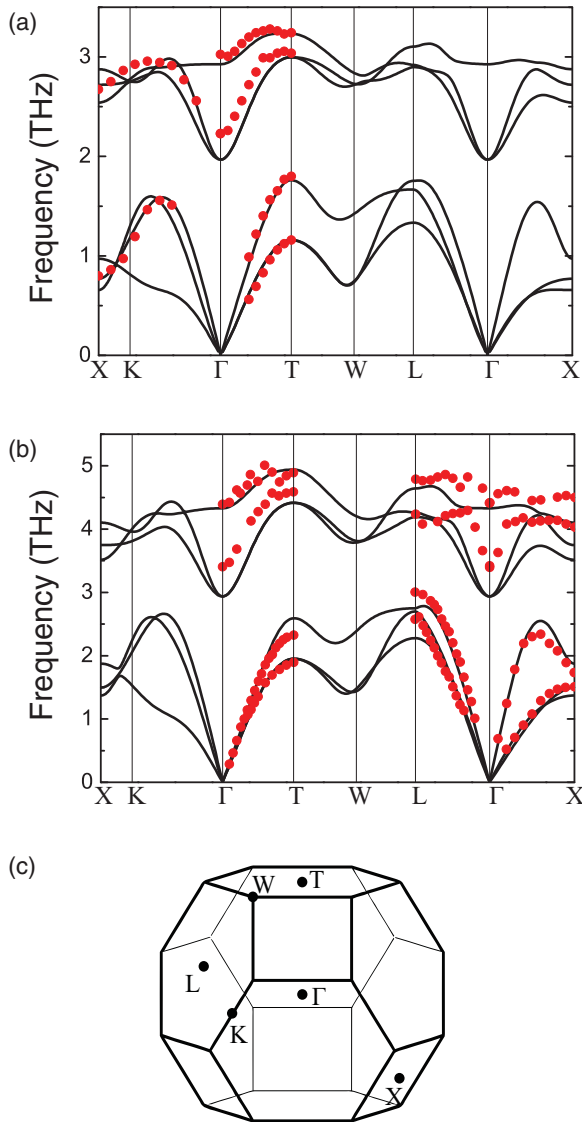


FIG. 3. (Color online) Phonon dispersion of (a) Bi and (b) Sb. Dots are experimental values from [37] for Bi and [38] for Sb. (c) The high symmetry points in the Brillouin zone.

second-order force constant tensors versus distance. Both Bi and Sb have the interactions of significant magnitude occurring at the ninth neighbors, which agree well with the previous reports [17,18]. In Fig. 3, the calculated phonon dispersions for Bi and Sb are compared with the experimental values. Both calculated phonon dispersions are similar to the experimental data, confirming the accuracy of the calculated second-order force constants.

Since the ninth neighbors in Bi and Sb have significant second-order force constants, the third-order force constants at the ninth neighbors should also be of interest. In Fig. 2(b), we plot the two-body third-order force constants as a function of distance. Each dot represents a third-order force constant. As seen in Fig. 2(b), the third-order force constants have substantial values at the ninth neighbors. The importance of the ninth-neighbor interaction on crystal anharmonicity can be checked with the mode Grüneisen parameters. The mode

Grüneisen parameters are calculated with the two different sets of third-order force constants: one includes up to the fourth neighbors and the other includes up to the 10th neighbors. To validate the third-order force constants, the reference mode Grüneisen parameters are also calculated. For the reference mode Grüneisen parameters, we used density functional perturbation theory to calculate the phonon frequencies for two different crystal volumes: a crystal at equilibrium and one with the volume increased by 1%. We then take the finite differences of the two different phonon frequencies and calculate the mode Grüneisen parameters from the definition $\gamma = -d \ln \omega / d \ln V$, where ω and V are a phonon frequency and a crystal volume, respectively. Shown in Fig. 4 are the calculated acoustic mode Grüneisen parameters. Figure 4 shows that the acoustic mode Grüneisen parameters are underestimated over a range of wave vectors when the third-order force constants are considered only up to the fourth neighbors. Even after considering up to the eighth neighbors, the mode Grüneisen parameters are relatively unchanged. This is consistent with the negligible third-order force constants at the fifth, sixth, seventh, and eighth neighbors, as shown in Fig. 2(b). However, when extending the range up to the 10th neighbors, the calculated acoustic mode Grüneisen parameters agree reasonably well with the reference Grüneisen

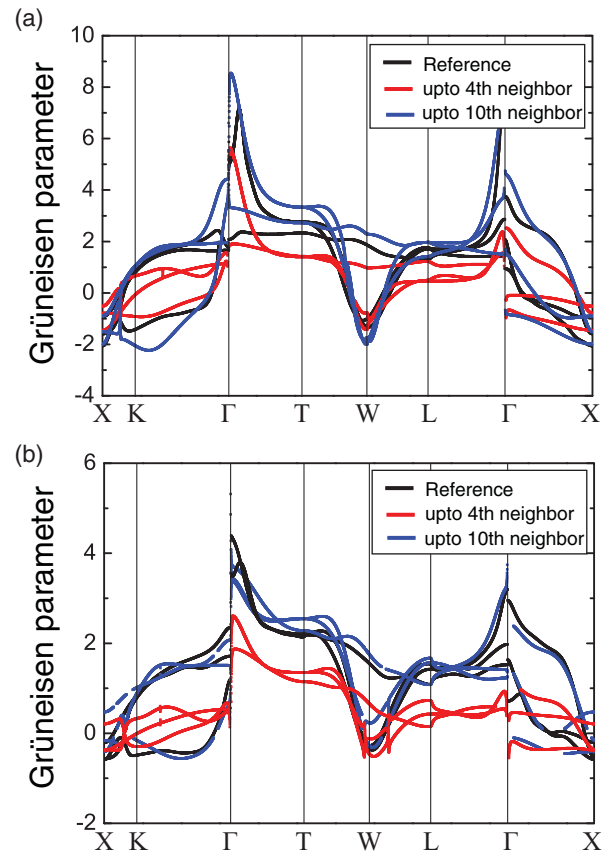


FIG. 4. (Color online) Acoustic mode Grüneisen parameters of (a) Bi and (b) Sb comparing inclusion up to the fourth and 10th neighbors to the references. The reference Grüneisen parameters are calculated using the difference of phonon frequencies of the two different crystal volumes.

parameters. This confirms that the ninth-neighbor interaction is playing a significant role in the anharmonic properties. The optical mode Grüneisen parameter was also determined from third-order force constants that included up to the fourth- and 10th-neighbor interaction terms. Both cases yielded similar values for the optical Grüneisen parameter.

The significant interaction at the ninth-nearest neighbors can be explained by the resonant bonding in Bi and Sb [26]. Bi and Sb have very weak *sp* hybridization, and the *s* band is well below the *p* band [27]. Therefore, *s* electrons do not participate in the chemical bonding, and we can consider only *p* electrons forming the chemical bonds. For the three *p* electrons per atom in Bi or Sb to meet the six coordination number requirement in the cubiclike crystal structure, the electrons alternate their positions among six chemical bonds, leading the chemical bonding called resonant bonding [28]. This resonant bonding picture implies two important features: (1) electrons are highly delocalized and are therefore easily polarized upon external perturbations, and (2) the chemical bonds in Bi and Sb are almost collinear due to the cubiclike crystal structure. The almost collinear bonding can be found in Fig. 1, as explained earlier. These two features result in the significant interaction at the ninth-nearest neighbors. The electron polarization by the displacement of the origin atom is long ranged along the collinear bonding direction due to the large electronic polarizability and almost collinear bonding. This long-ranged electron polarization reaches the ninth-nearest neighbors, giving rise to the significant interatomic interaction between the origin and the ninth-nearest neighbor atoms.

To study the effects of alloying on κ_{ph} , the virtual crystal approximation is used [29]. The atomic mass and the force constants of the virtual crystal were linearly interpolated between Bi and Sb, weighted by the composition ratio of the constituents. The lattice constant of the virtual crystal is also averaged according to the composition ratio, which is well justified by the fact that the Bi-Sb alloy follows Vegard's law [30]. Three-phonon scattering is calculated using the virtual crystal approximation, while the atomic mass disorder is treated as an additional elastic scattering mechanism. This approach is successful in predicting the Si-Ge alloy thermal conductivity [16].

III. SCATTERING RATE AND LATTICE THERMAL CONDUCTIVITY

The lattice thermal conductivity can be calculated from the distribution function of the phonon modes. We calculate the distribution function by solving the linearized Boltzmann equation with the scattering rates due to the three-phonon process and mass disorder. The scattering rate of the three-phonon process is given by

$$W_{1,2}^3 = 2\pi |V_3(-1, -2, 3)|^2 n_1^0 n_2^0 (n_3^0 + 1) \delta(-\omega_1 - \omega_2 + \omega_3) \quad \text{for coalescence processes} \quad (2)$$

$$W_1^{2,3} = 2\pi |V_3(-1, 2, 3)|^2 n_1^0 (n_2^0 + 1) (n_3^0 + 1) \delta(-\omega_1 + \omega_2 + \omega_3) \quad \text{for decay processes} \quad (3)$$

where 1, 2, and 3 denote phonon modes in the three-phonon process, while n^0 and ω indicate the Bose-Einstein equilibrium distribution function and the phonon frequency, respectively. The three-phonon scattering matrix element V_3 is given by

$$V_3(1, 2, 3) = \left(\frac{\hbar}{8N\omega_1\omega_2\omega_3} \right)^{1/2} \times \sum_{b_1 b_2 b_3} \sum_{\alpha\beta\gamma} \sum_{\mathbf{R}_2 \mathbf{R}_3} \Phi_{\alpha\beta\gamma}(\mathbf{0}b_1, \mathbf{R}_2 b_2, \mathbf{R}_3 b_3) \times e^{i\mathbf{q}_2 \cdot \mathbf{R}_2} e^{i\mathbf{q}_3 \cdot \mathbf{R}_3} \frac{e_{\alpha b_1} e_{\beta b_2} e_{\gamma b_3}}{\sqrt{m_{b_1} m_{b_2} m_{b_3}}} \quad (4)$$

where $\Phi_{\alpha\beta\gamma}(\mathbf{0}b_1, \mathbf{R}_2 b_2, \mathbf{R}_3 b_3)$ is a third-order force constant with Cartesian coordinates $\alpha\beta\gamma$ and $\mathbf{R}b$ representing the lattice vector and basis atom. Here, $e_{\alpha b}$ denotes the phonon eigenvector component of the basis atom b along direction α , while N is the total number of wave vectors in the first Brillouin zone. The mass disorder scattering rate is

$$W_1^2 = \frac{\pi}{2} g \omega_1 \omega_2 n_1^0 (n_2^0 + 1) \sum_b |\mathbf{e}_b^* \cdot \mathbf{e}_b|^2 \delta(\omega_1 - \omega_2) \quad (5)$$

with the mass variance factor g defined by $g = \sum_i f_i (1 - M_i/M_{\text{avg}})^2$, where f_i is the fraction of element i .

Putting both scattering rates above into the Boltzmann equation, we obtain

$$-\mathbf{v}_1 \cdot \nabla T \left(\frac{\partial n_1^0}{\partial T} \right) = \sum_{2,3} \left[W_{1,2}^3 (\Psi_1 + \Psi_2 - \Psi_3) + \frac{1}{2} W_1^{2,3} (\Psi_1 - \Psi_2 - \Psi_3) \right] + \sum_2 W_1^2 (\Psi_1 - \Psi_2) \quad (6)$$

where Ψ is a linearized deviation of the distribution function from equilibrium, defined as $\Psi = (n^0 - n)/(\partial n^0/\partial \beta)$ with $\beta = \hbar\omega/k_B T$. We solve the linearized Boltzmann equation above iteratively to find $\Psi/\nabla T$. The detailed procedure is provided in other papers [12]. In contrast to the iterative method mentioned above, a more commonly used method to solve the Boltzmann equation is to neglect Ψ_2 and Ψ_3 in Eq. (6), and this approximation is known as the single-mode relaxation time (SMRT) approximation. The SMRT assumes only one phonon mode is ever out of equilibrium. The time for the nonequilibrium mode to relax to equilibrium is then calculated. We used both the full iterative method and the SMRT approximation to calculate the lattice thermal conductivity from the Boltzmann equation, and we compare the results from the two methods. After solving the Boltzmann equation, the lattice thermal conductivity can be obtained by

$$\kappa_{\alpha\beta} = -\frac{1}{V} \sum_{BZ} \hbar \omega v_\alpha n^0 (n^0 + 1) \frac{\Psi_\beta}{\nabla_\beta T} \quad (7)$$

where α and β are Cartesian directions, V is the crystal volume, and v is the phonon group velocity.

One of the numerical uncertainties in this calculation occurs in the energy conservation of the scattering rate calculation. Due to the computational limitations, the Brillouin zone is sampled with a relatively coarse mesh. To find sets of three

phonons satisfying the energy and momentum conservation, each point in the coarse mesh is usually broadened by a Gaussian function. However, in this case, numerical uncertainties arise from the tuning of two adjustable parameters (mesh size and Gaussian width). To avoid this artifact, a tetrahedron method is utilized for the Brillouin zone integrations of δ functions [31]. With this method, the mesh size is the only adjustable parameter; consequently, the calculation should converge as the mesh size is increased. For our calculation, the mesh size of $16 \times 16 \times 16$ was suitable for convergence.

IV. RESULTS AND DISCUSSION

In Fig. 5(a), we show that the ninth-neighbor interaction has a significant effect on the lattice thermal conductivity. We compare the κ_{ph} in the binary direction calculated with the two different force constant sets: one set includes up to the 10th neighbor, and the other includes up to the fourth neighbor for the third-order force constants. In both cases, the second-order force constants include up to the 14th neighbor; otherwise, the phonon dispersion is not stable and the phonon frequencies of some modes have imaginary

values. As shown in the mode Grüneisen parameter plot (Fig. 4), when the ninth-neighbor interaction is not included for the third-order force constants, the crystal anharmonicity is largely underestimated. Figure 5(a) explicitly shows that the κ_{ph} is significantly overestimated when the ninth-neighbor interaction is not included for the third-order force constants. However, when the third-order force constants include up to the 10th-neighbor interactions, the calculated κ_{ph} is half of the value obtained when including only third-order force constants up to the fourth neighbor.

The calculated results with the ninth-neighbor interaction are validated by comparing these results to the previously reported experimental data [6,7]. Figure 5(a) shows that our calculation results with the ninth-neighbor interaction agree well with the experimental data by Uher and Goldsmid [6]. Our calculation is further confirmed by comparing to another measurement by Kagan and Red'ko [7], showing $\kappa_{\text{ph}} \approx 5 \text{ W/m-K}$ around 250 K. In contrast, another reported value for κ_{ph} by Gallo *et al.* [8], which is calculated from the difference between measured κ_{tot} and calculated κ_e , as briefly discussed later, shows disagreement with our calculation near room temperature. Our calculated κ_{ph} is twice the reported value [8] at room temperature. This disagreement could stem from the simple electron transport model used in the referenced paper [8]. Instead of directly measuring the lattice thermal conductivity, Gallo *et al.* obtained the electronic thermal conductivity from an electron transport model using a parabolic band structure and an electron scattering rate that obeys a simple power law. The measured Seebeck coefficient and electrical resistivity determine the electron contribution to the thermal conductivity, and then the lattice thermal conductivity is calculated by subtracting the deduced electronic thermal conductivity from the measured total thermal conductivity. To reiterate, our calculation near room temperature is well validated by Kagan and Red'ko's direct measurement [7].

We also see in Fig. 5(a) that the results from the SMRT approximation are similar to the calculations from the full iterative solution of the Boltzmann equation. This is because the temperatures in our calculations are large compared to the Debye temperature of Bi (120 K). When the temperature is not significantly smaller than the Debye temperature, umklapp scattering is dominant over normal scattering. In this case, the SMRT is usually a good approximation.

In Fig. 5(b), we compare the binary (\perp) and the trigonal (\parallel) directions of Bi in terms of κ_{ph} . The previous paper based on obtaining the electronic thermal conductivity [8], mentioned above, estimates that $\kappa_{\text{ph},\parallel}$ is half of the value of $\kappa_{\text{ph},\perp}$ in Bi at room temperature. Our calculation shows values for $\kappa_{\text{ph},\parallel}$ is smaller than for $\kappa_{\text{ph},\perp}$, but the difference is less than 10%. The relative value of $\kappa_{\text{ph},\parallel}$ compared to $\kappa_{\text{ph},\perp}$ can be explained by the fact that the rhombohedral structure of Bi is close to the cubic structure but slightly stretched along the trigonal direction. Therefore, the atomic bonding is slightly softer in the trigonal direction than in the binary direction, resulting in the lower lattice thermal conductivity in the trigonal direction. However, the distortion from the exact cubic structure is very small: the rhombohedral angle of Bi (α in Fig. 1) is $57^\circ 30'$, similar to 60° for the exact cubic structure [30]. This very small distortion explains the almost isotropic κ_{ph} of Bi shown in Fig. 5(b). The almost isotropic lattice thermal conductivity

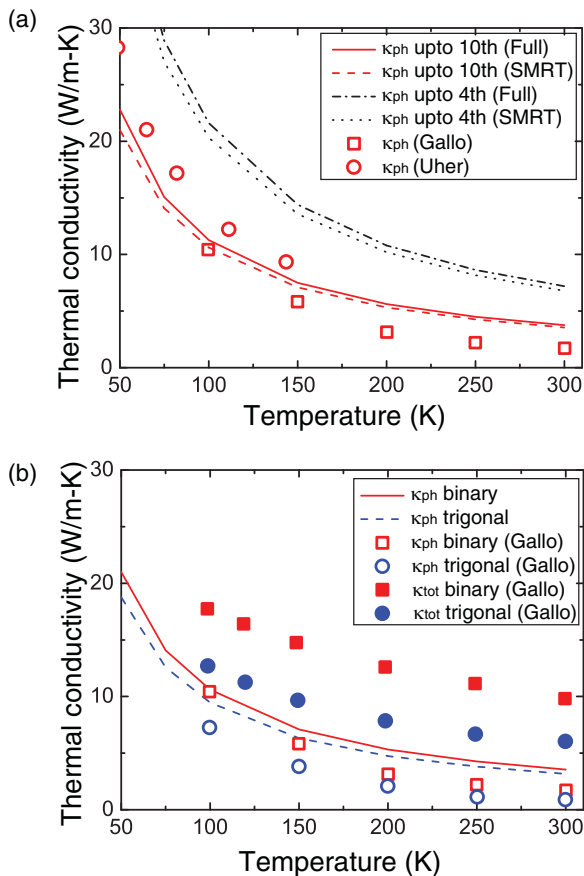


FIG. 5. (Color online) Thermal conductivity of Bi (a) in the binary direction and (b) in comparison between the binary and the trigonal directions. κ_{ph} in (b) is calculated with the SMRT approximation and using third-order force constants up to the 10th neighbors. The solid lines and dots represent our first-principles calculation results and the experimental data from the literature, respectively.

of Bi is in contrast with its well-known highly anisotropic electron transport properties [5]. This shows that the small distortion of crystal structure of Bi affects the electron and the phonon transport to a different extent. Even though the distortion of the Bi crystal structure is very small from the exact cubic structure, this small distortion causes highly anisotropic shapes to occur in the very small electron and hole pockets responsible for its electronic transport properties, giving rise to largely anisotropic electron transport behavior. However, the small distortion does not much affect the lattice vibrational properties; thus, κ_{ph} is observed to be almost isotropic.

We also compare the κ_{ph} and κ_{tot} of Bi in Fig. 5(b) to estimate the relative contributions from phonons and electrons to κ_{tot} . In the binary direction, $\kappa_{\text{ph},\perp}$ is $\sim 60\%$ of $\kappa_{\text{tot},\perp}$ at 100 K, and its contribution decreases with temperature. In the trigonal direction, the phonon contribution from $\kappa_{\text{ph},\parallel}$ to $\kappa_{\text{tot},\parallel}$ is more significant than in the binary direction, with a contribution of $\sim 75\%$ at 100 K. Based on this large contribution from phonons with $\kappa_{\text{ph},\parallel}$ to $\kappa_{\text{tot},\parallel}$, we conclude here that it can be possible to reduce the thermal conductivity effectively by enhancing phonon scattering, as recently demonstrated in $\text{Bi}_{1.4}\text{Sb}_{0.6}\text{Te}_3$ and PbTe [32,33]. In particular, the large lattice contribution in the trigonal direction would be interesting, because the electron transport in this direction of Bi has a favorable feature for a high thermoelectric power factor. The electrons in the trigonal direction of Bi have an extremely large value for the product of mobility and the density-of-states effective mass, $\mu(m^*/m)^{3/2}$, due to the high anisotropy in its electronic structure, which is directly related to the thermoelectric power factor [5].

Many features of κ_{ph} in Sb, presented in Fig. 6, show strong similarities to the thermal conductivity of Bi. The ninth-neighbor interaction in Sb is also significant, and the κ_{ph} is significantly overestimated without including this contribution in the calculation. The SMRT is a good approximation for Sb since its Debye temperature is also small (~ 200 K). The distortion from the exact cubic structure is also small for Sb, as it is in Bi, resulting in an almost isotropic κ_{ph} . The most noticeable difference between Bi and Sb is the contribution of κ_{ph} to κ_{tot} , comparing Figs. 5(b) and 6(b). The κ_{ph} contribution is comparable to the κ_e in Bi, but the κ_{ph} contributes only a small portion of κ_{tot} in Sb. In other words, κ_e is significant in Sb, because the carrier density in Sb is two orders of magnitude larger than that of Bi [34].

The κ_{ph} of Bi, Sb, and Bi-Sb alloys is presented in Fig. 7. Our calculation for $\text{Bi}_{88}\text{Sb}_{12}$ agrees well with the experimental data for the κ_{ph} by Kagan and Red'ko [7], showing ~ 3 W/m-K around 100 K and ~ 2 W/m-K around 250 K for $\text{Bi}_{87}\text{Sb}_{13}$. Figure 7(a) shows that the κ_{ph} of Bi can be significantly reduced by alloying with small concentrations of Sb. The composition $\text{Bi}_{88}\text{Sb}_{12}$, which has the highest ZT among the Bi-Sb alloys, has four times smaller κ_{ph} than Bi at 100 K. In order to study the anisotropy of phonon transport, we compare the κ_{ph} in the binary and trigonal directions. The Bi-Sb alloy, like its Bi and Sb constituents, has a smaller κ_{ph} in the trigonal direction, but the difference between the trigonal and the binary directions is very small, indicating a predominantly isotropic κ_{ph} .

The comparison of κ_{tot} and κ_{ph} in Figs. 7(b) and 7(c) indicates whether electrons or phonons are the predominant heat carrier in Bi, Sb, and $\text{Bi}_{88}\text{Sb}_{12}$. Unlike Bi and Sb, the κ_{tot}

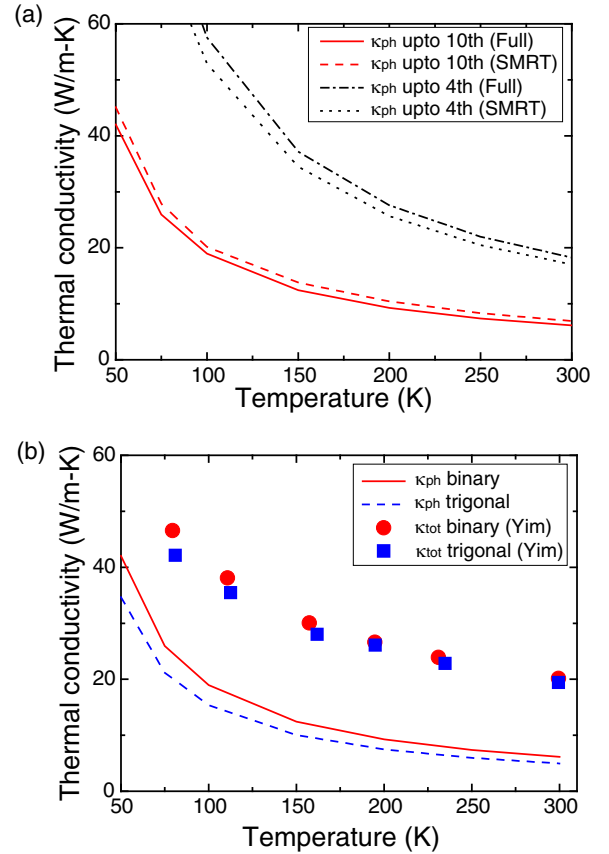


FIG. 6. (Color online) Thermal conductivity of Sb (a) in the binary direction and (b) in comparison between the binary and the trigonal directions. The solid lines and dots in (b) represent our first-principles calculation results and the experimental data from the literature, respectively.

of $\text{Bi}_{88}\text{Sb}_{12}$ comes predominantly from lattice contributions at low temperature. Around 75 K, the calculated κ_{ph} of $\text{Bi}_{88}\text{Sb}_{12}$ is comparable to the measured κ_{tot} for either the trigonal or the binary direction. The κ_e , in this case, is expected to be small due to the positive electronic band gap (~ 30 meV) of $\text{Bi}_{88}\text{Sb}_{12}$ [34]. The number of charge carrier in $\text{Bi}_{88}\text{Sb}_{12}$ is much less than that in Bi and Sb, resulting in the smaller κ_e . However, from comparing the measured κ_{tot} and the calculated κ_{ph} , the κ_e increases with temperature. This can be explained by the increasing charge carrier density and increasing bipolar thermal transport as temperature increases. From Fig. 7(c), the κ_e becomes comparable to the κ_{ph} near room temperature. Another noticeable feature in κ_{ph} of $\text{Bi}_{88}\text{Sb}_{12}$ is that its insensitivity to temperature variation. This is because mass disorder scattering, a temperature-independent process, is the dominant phonon scattering mechanism in this alloy.

Finally, we show in Fig. 8 the accumulated thermal conductivity versus phonon mean free path. This accumulated thermal conductivity is defined as [35,36]

$$\kappa_{\text{acc}}(\Lambda) = \sum_{\mathbf{q}\lambda} \kappa_{\mathbf{q}\lambda} \chi(\Lambda) \quad (8)$$

where $\kappa_{\mathbf{q}\lambda}$ represents the thermal conductivity of the phonon mode with wave vector \mathbf{q} and polarization λ . Here, Λ is

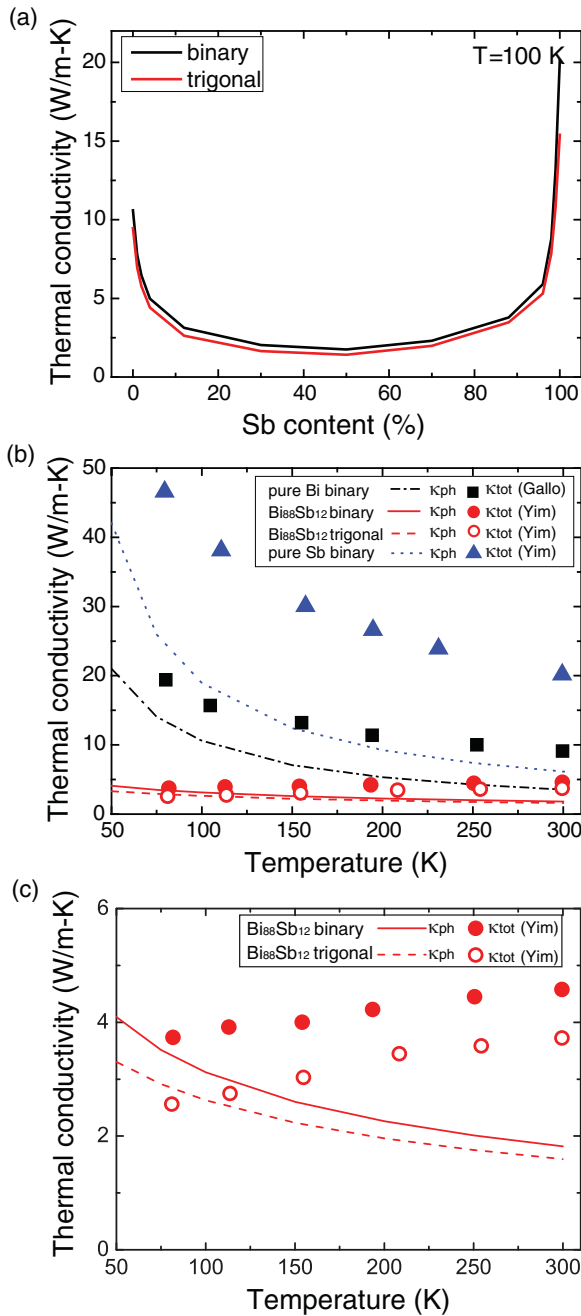


FIG. 7. (Color online) Thermal conductivity of the Bi-Sb alloys: (a) the effect of Sb content on the lattice thermal conductivity of Bi-Sb alloys; (b) comparison between the total and the lattice thermal conductivities of Bi, Sb, and Bi₈₈Sb₁₂; and (c) an enlarged plot for the Bi₈₈Sb₁₂ data along the binary and trigonal directions.

phonon mean free path, and $\chi(\Lambda)$ is a step function: $\chi(\Lambda) = 1$ when $\Lambda_{q\lambda} < \Lambda$, and $\chi(\Lambda) = 0$ otherwise. The accumulated thermal conductivity shows the range of mean free paths of the phonon modes that significantly contribute to thermal transport [35,36]. From Fig. 8(a), we see that most of the heat is carried by phonons with mean free paths ranging from 10 to 100 nm at 100 K. However, the phonon mean free path range of the Bi₈₈Sb₁₂ alloy is slightly different from that of Bi in the 50- to 100-nm region in Fig. 8(b): the mean free path range of

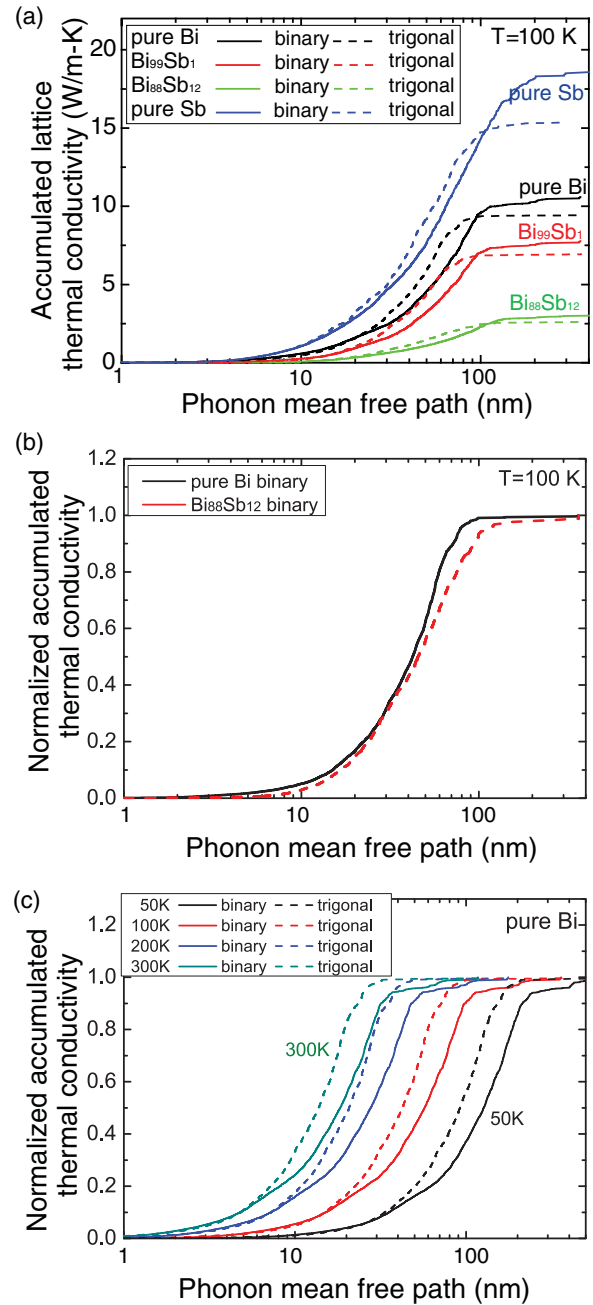


FIG. 8. (Color online) Phonon mean free path distribution of (a) Bi, Bi₉₉Sb₁, Bi₈₈Sb₁₂, and Sb at 100 K; (b) Bi and Bi₈₈Sb₁₂ at 100 K; and (c) Bi at 50, 100, 200, and 300 K for the binary and trigonal directions. In (b) and (c), the accumulated thermal conductivity is normalized by the lattice thermal conductivity value.

the alloy is extended to longer mean free paths compared to Bi. This is because the alloy scattering is effective for high-frequency phonons but not as effective for low-frequency phonons. If the alloy scattering is approximated by a point defect scattering mechanism, the Rayleigh scattering model shows that the scattering rate is proportional to the fourth power of phonon frequency.

Figure 8(a) shows that the nanostructures in the 10- to 100-nm range scale can significantly contribute to phonon scattering, ultimately resulting in a greatly reduced thermal

conductivity in both the Bi and Bi-Sb alloys. In addition to the reduction in κ_{ph} , it is known that Bi nanowires become semiconducting and exhibit a high power factor when the diameter is on the order of 10 nm [3,4]. If harmonic and anharmonic force constants of Bi nanowires are not drastically different from those of bulk phase Bi, the phonon mean free path distribution from bulk Bi calculations can guide the design of Bi nanowires for high ZT . To provide a strategy for reducing κ_{ph} through nanostructuring, we present the phonon mean free path distributions of Bi at various temperatures in Fig. 8(c). From Fig. 8(c), we see that nanostructures having characteristic sizes of ~ 10 nm would be effective for suppressing κ_{ph} in the temperature range of 100 to 300 K, because they are expected to reduce the lattice thermal conductivity by a factor of 10 at 100 K to a factor of 3 at 300 K if boundary scatterings are assumed to be completely diffuse.

V. CONCLUSIONS

We calculate the lattice thermal conductivities of Bi, Sb, and Bi-Sb alloys from first principles. We explicitly show that the significant ninth-neighbor interaction is important for anharmonic interatomic force constants, phonon scattering, and lattice thermal conductivity. Our calculation agrees well with the experimental lattice thermal conductivity values for the binary direction. We also provide the lattice thermal conductivity values for the trigonal direction, which has not been directly measured. From our calculation, the lattice thermal conductivities are almost isotropic in Bi, showing a significant contrast with its highly anisotropic electron transport. This implies that the small distortion in the crystal

structure can affect the electron and the phonon transport to a much different extent. By comparing our calculated lattice thermal conductivity to the measured total thermal conductivity, we compare the relative thermal conductivity contributions from phonons and electrons. The lattice thermal conductivity is comparable in magnitude to the electronic thermal conductivity in Bi. In Sb, however, the electronic contribution to the thermal conductivity is much more dominant because of the larger charge carrier concentration. In $\text{Bi}_{88}\text{Sb}_{12}$, the lattice thermal conductivity is the dominant contributor below 75 K but it becomes less significant as the temperature increases. Finally, we calculate the phonon mean free path distributions at various temperatures, providing a useful guide in determining appropriate nanostructure sizes for achieving significant lattice thermal conductivity reduction.

ACKNOWLEDGMENTS

We thank J. Garg and D. Broido for useful discussions. This paper was partially supported by Solid State Solar-Thermal Energy Conversion Center, an Energy Frontier Research Center funded by the U.S. Department of Energy, Office of Science, Office of Basic Energy Sciences, under Award No. DE-SC0001299/DE-FG02-09ER46577 for methodology development (K.E., M.S.D., and J.M.) and partially supported by the U.S. Department of Defense, Air Force Office of Scientific Research, Multidisciplinary University Research Initiative, via Ohio State University (S.L. and G.C.). S.L. acknowledges support from a Samsung scholarship.

-
- [1] W. M. Yim and A. Amith, *Solid-State Electron.* **15**, 1141 (1972).
 - [2] K. Behnia, M.-A. Méasson, and Y. Kopelevich, *Phys. Rev. Lett.* **98**, 076603 (2007).
 - [3] J. P. Heremans, C. M. Thrush, D. T. Morelli, and M.-C. Wu, *Phys. Rev. Lett.* **88**, 216801 (2002).
 - [4] Y.-M. Lin, X. Sun, and M. S. Dresselhaus, *Phys. Rev. B* **62**, 4610 (2000).
 - [5] G. S. Nolas, J. Sharp, and H. J. Goldsmid, *Thermoelectrics: Basic Principles and New Materials Developments* (Springer, New York, 2001).
 - [6] C. Uher and H. J. Goldsmid, *Phys. Status Solidi B* **65**, 765 (1974).
 - [7] V. D. Kagan and N. A. Red'ko, *Sov. Phys. JETP* **73**, 664 (1991) [*Zh. Eksp. Teor. Fiz.* **100**, 1205 (1991)].
 - [8] C. F. Gallo, B. S. Chandrasekhar, and P. H. Sutter, *J. Appl. Phys.* **34**, 144 (1963).
 - [9] G. S. Nolas and H. J. Goldsmid, in *Thermal Conductivity: Theory, Properties, and Applications*, edited by T. M. Tritt (Kluwer, New York, 2004).
 - [10] D. A. Broido, M. Malorny, G. Birner, N. Mingo, and D. A. Stewart, *Appl. Phys. Lett.* **91**, 231922 (2007).
 - [11] A. Ward and D. A. Broido, *Phys. Rev. B* **81**, 085205 (2010).
 - [12] A. Ward, D. A. Broido, D. A. Stewart, and G. Deinzer, *Phys. Rev. B* **80**, 125203 (2009).
 - [13] T. Luo, J. Garg, J. Shiomi, K. Esfarjani, and G. Chen, *Europhys. Lett.* **101**, 16001 (2013).
 - [14] L. Lindsay, D. A. Broido, and T. L. Reinecke, *Phys. Rev. B* **87**, 165201 (2013).
 - [15] K. Esfarjani, G. Chen, and H. T. Stokes, *Phys. Rev. B* **84**, 085204 (2011).
 - [16] J. Garg, N. Bonini, B. Kozinsky, and N. Marzari, *Phys. Rev. Lett.* **106**, 045901 (2011).
 - [17] L. E. Díaz-Sánchez, A. H. Romero, and X. Gonze, *Phys. Rev. B* **76**, 104302 (2007).
 - [18] É. D. Murray, S. Fahy, D. Prendergast, T. Ogitsu, D. M. Fritz, and D. A. Reis, *Phys. Rev. B* **75**, 184301 (2007).
 - [19] K. Esfarjani and H. T. Stokes, *Phys. Rev. B* **77**, 144112 (2008).
 - [20] X. Gonze, B. Amadon, P.-M. Anglade, J.-M. Beuken, F. Bottin, P. Boulanger, F. Bruneval, D. Caliste, R. Caracas, M. Côté *et al.*, *Comput. Phys. Comm.* **180**, 2582 (2009).
 - [21] C. Hartwigsen, S. Goedecker, and J. Hutter, *Phys. Rev. B* **58**, 3641 (1998).
 - [22] L. E. Díaz-Sánchez, A. H. Romero, M. Cardona, R. K. Kremer, and X. Gonze, *Phys. Rev. Lett.* **99**, 165504 (2007).
 - [23] Z. Tian, K. Esfarjani, and G. Chen, *Phys. Rev. B* **86**, 235304 (2012).
 - [24] X. Gonze and C. Lee, *Phys. Rev. B* **55**, 10355 (1997).
 - [25] X. Gonze, *Phys. Rev. B* **55**, 10337 (1997).
 - [26] S. Lee, K. Esfarjani, T. Luo, J. Zhou, Z. Tian, and G. Chen (unpublished).
 - [27] M. H. Cohen, L. M. Falicov, and S. Golin, *IBM J. Res. Dev.* **8**, 215 (1964).

- [28] G. Lucovsky and R. M. White, *Phys. Rev. B* **8**, 660 (1973).
- [29] B. Abeles, *Phys. Rev.* **131**, 1906 (1963).
- [30] P. Cucka and C. S. Barrett, *Acta Crystallogr.* **15**, 865 (1962).
- [31] Ph. Lambin and J. P. Vigneron, *Phys. Rev. B* **29**, 3430 (1984).
- [32] B. Poudel *et al.*, *Science* **320**, 634 (2008).
- [33] K. Biswas, J. He, I. D. Blum, C.-I. Wu, T. P. Hogan, D. N. Seidman, V. P. Dravid, and M. G. Kanatzidis, *Nature* **489**, 414 (2012).
- [34] J.-P. Issi, *Aust. J. Phys.* **32**, 585 (1979).
- [35] C. Dames and G. Chen, in *Handbook of Thermoelectrics: Macro to Nano*, edited by D. M. Rowe (CRC Press, Boca Raton, Florida, 2006).
- [36] A. S. Henry and G. Chen, *J. Comput. Theor. Nanosci.* **5**, 141 (2008).
- [37] J. L. Yarnell, J. L. Warren, R. G. Wenzel, and S. H. Koenig, *IBM J. Res. Dev.* **8**, 234 (1964).
- [38] R. I. Sharp and E. Warming, *J. Phys. F* **1**, 570 (1971).